Title
A conformational switch in HP1 releases auto-inhibition to drive heterochromatin assembly.

Journal
Nature, 496(7445)

Authors
Liao, Maofu
Naber, Nariman
Pate, Edward
et al.

Publication Date
2013-04-18

DOI
10.1038/nature12032

Peer reviewed

Published in final edited form as:
Nature. 2013 April 18; 496(7445): 377–381. doi:10.1038/nature12032.

A conformational switch in HP1 releases auto-inhibition to drive heterochromatin assembly

Daniele Canzio[1,2], **Maofu Liao**[1], **Nariman Naber**[1], **Ed Pate**[3], **Adam Larson**[1,4], **Shenping Wu**[1], **Diana B. Marina**[1,4], **Jennifer F. Garcia**[1,4], **Hiten D. Madhani**[1], **Roger Cooke**[1], **Peter Schuck**[5], **Yifan Cheng**[1], and **Geeta J. Narlikar**[1,*]

[1]Department of Biochemistry and Biophysics, University of California San Francisco, 94158, USA.

[2]Chemistry and Chemical Biology Graduate Program University of California San Francisco, 94158,USA.

[3]Voiland School of Chemical Engineering and Bioengineering, Washington State University, Pullman, WA, 99164 USA.

[4]Tetrad Graduate Program University of California San Francisco, 94158, USA.

[5]National Institute of Biomedical Imaging and Bioengineering, National Institute of Health, Bethesda, MD, 20892, USA.

Abstract

A hallmark of histone H3 lysine 9 (H3K9) methylated heterochromatin, conserved from fission yeast,*Schizosaccharomyces pombe* (*S. pombe*), to humans, is its ability to spread to adjacent genomic regions[1–6]. Central to heterochromatin spread is the heterochromatin protein 1 (HP1), which recognizes H3K9 methylated chromatin, oligomerizes, and forms a versatile platform that participates in diverse nuclear functions, ranging from gene silencing to chromosome segregation[1–6]. How HP1 proteins assemble on methylated nucleosomal templates and how the HP1-nucleosome complex achieves functional versatility remain poorly understood. Here, we show that binding of the major *S. pombe* HP1 protein, Swi6, to methylated nucleosomes drives a switch from an auto-inhibited state to a spreading competent state. In the auto-inhibited state, a histone mimic sequence in one Swi6 monomer blocks methyl mark recognition by the chromodomain of another monomer. Auto-inhibition is relieved by recognition of two template features, the H3K9 methyl mark and nucleosomal DNA. Cryo-Electron Microscopy (EM) based reconstruction of the Swi6-nucleosome complex provides the overall architecture of the spreading-competent state in which two unbound chromodomain sticky ends appear exposed. Disruption of

*To whom correspondence should be addressed: geeta.narlikar@ucsf.edu.

The authors declare no competing financial interests.

Author Contributions

D.C. and G.J.N identified, developed and addressed the core questions. D.C. performed the bulk of the experiments. P.S. trained D.C. in the use of AUC approaches and was instrumental in interpreting the AUC data. N.N. performed the EPR experiments. D.B. M. trained D.C. in strain construction and in the use of *S.pombe* assays. J.F.G. constructed some of the *S.pombe* strains and performed initial *in vivo* experiments. E.P., R.C., A.L. and D.C. deconvolved the EPR spectra. S.W. generated the cryo-EM reconstruction of the nucleosome alone. M.L. generated the EM reconstructions of the Swi6-nucleosome complex and the 2D reconstructions of the CFP-Swi6 and Swi6-CFP constructs. M.L., S.W. and Y.C. analyzed the EM data. Y.C. oversaw all the EM studies. H.D.M oversaw the design and interpretation of the *in vivo* experiments. R.C. oversaw the EPR analysis and interpretation. D.C. and G.J.N wrote the bulk of the manuscript with substantial intellectual contributions from R.C.

Supplementary Figures and Figure Legends

Supplementary Figures and Figure Legends (1-9) are described in the Supplementary Information.

Supplementary Discussion

Further discussion about (i) the rationale for the design of the Swi6 mutants, and (ii) the model for Swi6 binding to nucleosomes are described in the Supplementary Discussion.

the switch between the auto-inhibited and spreading competent state disrupts heterochromatin assembly and gene silencing *in vivo*. These findings are reminiscent of other conditionally activated polymerization processes, such as actin nucleation, and open up a new class of regulatory mechanisms that operate on chromatin *in vivo*.

HP1 has two structured domains, a chromodomain (CD) and a chromoshadow domain (CSD), connected by an unstructured hinge region (H) (Fig. 1a). The CD recognizes the H3K9me3 mark [7–9], while the CSD can homodimerize [10–12] and binds specific protein sequences [13,14]. The hinge is implicated in sequence-independent RNA and DNA binding [15,16]. Here we investigate how, the major *S. pombe* HP1 protein, Swi6, utilizes its different domains to create a regulatable HP1-chromatin complex.

It is hypothesized that heterochromatin spread relies on the ability of HP1 proteins to self-associate on chromatin [1,5]. To understand how Swi6 self-association is regulated by chromatin, we first characterized the individual oligomerization equilibria in the absence of nucleosomes using Analytical Ultracentrifugation (AUC). Previous work has characterized at least three Swi6 oligomeric states: a monomer, a dimer mediated by CSD-CSD interactions, and higher-order oligomers mediated by CD-CD interactions between dimers [10,12,15,17,18]. Analysis of our AUC data best describes the system as a two-step self-association process: a tight association of two Swi6 monomers with an affinity constant, K_{obs}^{dim}, $\left(1/K_{obs}^{dim} < \mathrm{lnM}, \quad \mathrm{at} \quad 8^{\circ}\mathrm{C}\right)$, followed by progressive self-association of Swi6 dimers with an identical chain elongation affinity constant, K_{obs}^{iso}, $\left(1/K_{obs}^{iso} \sim 70\mu\mathrm{M}, \quad \mathrm{at} \quad 8^{\circ}\mathrm{C}\right)$ (Fig. 1b, c, d and Supplementary Fig. 1, 2 and 3). This process, also known as isodesmic self-association, is analogous to the self-association of tubulin dimers [19].

We next tested if the most distinguishing feature of the chromatin template, the H3K9 methyl mark, increases Swi6 oligomerization when it occupies the CD. An increase in oligomerization, would be reflected by an increase in the overall weighted average sedimentation coefficient (S_W) of Swi6 as a function of H3K9me3 peptide (Fig. 1e). In contrast to our simplest expectation, addition of the methylated peptide reduced the value of S_W, implying that Swi6 self-association is inhibited by the methylated H3 tail peptide (Fig. 1e). This result suggested that the methylated H3-tail peptide and the CD-CD interface may compete for the same site. We noticed that the CD of Swi6 contains a sequence ($ARK_{94}GGG$) on a loop that resembles the amino acid sequence of the H3-tail surrounding the K9 position (ARK_9STG) (Fig. 1f). Interestingly, while the Swi6 sequence degenerates in higher organisms to just the lysine and proximal glycine (Fig. 1f), in human HP1 isoforms the lysine shows post-translation modifications found on H3K9 such as monomethylation and acetylation [20]. We therefore hypothesized that the ARK loop from the CD of one Swi6 could occupy the H3K9 binding site in another CD to mediate CD-CD self-association in solution (Fig. 1g). This is reminiscent of observations that the HP1 CD can bind ARK-containing motifs in histone H1 and G9a proteins [21,22].

To test this model, we investigated the effects of replacing the R93 and the K94 residues with alanines ($Swi6^{LoopX}$, Fig. 1g, Supplementary Table 1) on oligomerization. As predicted by the model, the $Swi6^{LoopX}$ mutant showed a small but reproducible decrease in the isodesmic affinity constant $\left(K_{obs}^{iso}\right)$ (Fig. 2a and Supplementary Fig 4, 3-fold). Interestingly, we noticed a substantially larger reduction in the association constant for dimerization $\left(K_{obs}^{dim}\right)$ (Fig. 2b and Supplementary Fig 4, 14-fold). Thus, in addition to the previously identified CSD-CSD interface, the ARK loop-CD interaction also participates in stabilizing a Swi6 dimer. We further found that $Swi6^{LoopX}$ binds tail peptides ~6-fold more strongly

than Swi6^{WT} (Fig 2d), and that Swi6 dimerization is weakened with saturating methylated H3 tail peptide (Supplementary Fig. 4). These results indicate that the ARK loop-CD interaction is mutually exclusive with H3 tail binding.

The above data suggest that a Swi6 dimer can exist in at least two states: a closed state in which the ARK loop engages the CD of its partner Swi6 and an open state in which the ARK loop-CD interaction is broken (Fig. 2c). Self-association of dimers then consists of: (1) a conformational step between closed and open states (K^{conf}) and (2) a self-association step between dimers in the open state (K^{oligo}). For Swi6^{WT} the measured isodesmic association step (K_{obs}^{iso}) is a product of K^{conf} and K^{oligo} (Fig. 2c). In Swi6^{LoopX} the effect on dimerization masks the destabilizing effect of the loop mutations on the actual oligomerization step (K^{oligo}) (Fig. 2c).

To investigate the extent of similarity between the loop-CD interaction and the H3-CD interaction, we used two additional mutants. The first is Swi6^{CageX}, in which an aromatic cage residue important for H3K9me3 binding [8] is mutated to alanine (Fig. 1g, Supplementary Table 1). The second is Swi6^{AcidicX}, in which an acidic stretch N-terminal to the first aromatic cage residue of the CD, is mutated to alanines (Fig. 1g, Supplementary Table 1, and rationale in Supplementary Discussion). Both mutants show reduced binding to H3K9me3 peptides (Fig. 2d). These mutants also destabilize Swi6 oligomerization and dimerization (Fig. 2a and b, Supplementary Fig 4), suggesting that similar interactions are involved in the H3-CD and ARK loop-CD interfaces (Fig. 1g).

We next used Electron Paramagnetic Resonance (EPR) spectroscopy to ask whether disruption of the loop-CD interface or binding of the H3K9me3 tail makes the loop more mobile by stabilizing the open conformation (Fig. 2c and 2e). Changes in the mobility of a site-specifically attached spin probe can give well-defined changes in its EPR spectrum [23]. We mutated all three native cysteines in Swi6 to serines (Swi6^{3S}, Supplementary Table 1), mutated the G95 residue on the loop to a cysteine and then modified it with a maleimide spin probe (Swi6^{probe}, Supplementary Table 1). Mutating the native cysteines destabilized oligomerization, H3 peptide binding, and nucleosome binding (Supplementary Fig. 5) but the mutants still showed significant discrimination for the H3K9 methyl mark (Supplementary Fig. 5).

Two spectral components were observed for Swi6$^{probe\text{-}WT}$, one with higher mobility and one with reduced mobility. Deconvolution of the two components gave the fraction of probes that are immobilized. In parallel, AUC experiments confirmed the oligomeric state of the protein. For the Swi6$^{probe\text{-}WT}$ protein ~35% of the probes were immobile (Fig. 2f). Compared to Swi6$^{probe\text{-}WT}$, the fraction of immobile probes decreased in Swi6$^{probe\text{-}LoopX}$, Swi6$^{probe\text{-}AcidicX}$ and Swi6$^{probe\text{-}DimerX}$ (L315D, Supplementary Table 1), which disrupts CSD-CSD dimerization and increases monomeric Swi6 [18] (Fig. 2f; and Supplementary Fig. 5). The values obtained for the mutants relative to WT are consistent with our thermodynamic characterization (Fig. 2a and 2b). Further, as predicted by the model (Fig. 2c and 2e), addition of the H3K9me3 peptide decreased the fraction of immobile probes. The H3K9me3 peptide was ~100-fold better at decreasing the immobile probe fraction compared to both, H3K9 and H3K4me3 peptides, indicating that the effect was specific for the H3K9me3 mark (Fig. 2g, additional mutants in Supplementary Fig. 5).

To investigate the global structure of Swi6 dimers, we used negative stain EM. To increase the mass for visualization by EM, and to identify the N-terminus of Swi6, we fused a Cyan Fluorescent Protein (CFP) molecule to the N-terminus of Swi6 (Fig. 3a and Supplemental Fig. 6). The CFP-Swi6 construct showed an extended conformation (Fig. 3a). We reasoned that the proximity of the CFP-tag to the CD perhaps disrupts the loop-CD interaction.

Consistent with this reasoning CFP-Swi6 forms a ~10-fold weaker dimer than $Swi6^{WT}$ (Supplementary Fig. 6 and Fig. 2b). To maintain the loop-CD interaction, we moved the CFP tag to the C-terminus (Fig. 3b). Swi6-CFP has a similar dimerization constant as $Swi6^{WT}$, consistent with having an intact ARK loop-CD interaction (Supplementary Fig. 6), shows a more condensed structure compared to CFP-Swi6 and has a lower sedimentation coefficient (Fig. 3b and Supplemental Fig. 6). These results raised the possibility that the extended conformation of CFP-Swi6 reflects the open state (Fig. 2c), which is capable of binding methylated nucleosomes. We therefore visualized Swi6 bound to a methylated nucleosome using cryo-EM, and for comparison, visualized nucleosomes alone (Fig. 3c). Based on our previous biochemical knowledge we applied 2-fold symmetry to the Swi6-nucleosome complex to obtain the three-dimensional (3D) reconstruction (see also Supplementary Methods). For the nucleosome and the Swi6-nucleosome complex, 3D reconstructions were calculated using the nucleosome structure as an initial model to an overall resolution of ~15Å and ~25Å, respectively (Fig. 3c, Supplementary Fig. 7, and Methods).

The 25Å resolution of the Swi6-nucleosome complex precludes conclusions about the detailed conformations of the bound Swi6 dimers. We instead further analyzed the difference density between the complex and nucleosome (Fig. 3c). While we cannot rule out that Swi6 binding alters nucleosome conformation, the difference density has roughly the mass (~125kDa) of two Swi6 dimers (~150 kDa) as determined previously [18]. We thus assume that the difference density is mainly contributed by the bound Swi6 dimers. The putative location of the CD suggests that one CD engages an H3 tail and one CD protrudes out in solution (Fig. 3d). This arrangement of the CDs is compatible with the sticky ends architecture proposed previously (Fig. 3e) [18]. The putative location of the CSD dimer suggests that this domain may also engage the nucleosome (Fig. 3c and d). This possibility has also been previously suggested [24–26]. To directly test it, we measured binding of the $Swi6^{DimerX}$ to H3K9me3 nucleosomes, and observed that disruption of the CSD dimer decreases binding by 10-fold (Fig. 4a and Supplementary Fig. 8).

Surprisingly, in contrast to the results with the H3 tail peptides (Fig. 2d), disrupting the auto-inhibition via the $Swi6^{LoopX}$ mutant reduced binding to methylated nucleosomes by 10-fold, even though discrimination for the methyl mark was maintained (Fig. 4a and Supplementary Fig. 8). This suggested that, when displaced from the CD, the ARK loop may help Swi6 make additional interactions with the nucleosome. We tested if the positively charged ARK loop assists interactions with DNA. We found that $Swi6^{WT}$ binds ~4-fold tighter than $Swi6^{LoopX}$ to a 20 bp DNA (Fig. 4b). Further, $Swi6^{WT}$ bound to the DNA ~4-fold tighter with saturating H3K9me3 peptide, consistent with the loop being available when displaced from the CD (Fig. 4b and Supplementary Fig. 8). In contrast to $Swi6^{LoopX}$, $Swi6^{AcidicX}$, which binds H3K9me3 peptides more weakly than $Swi6^{WT}$, also binds methylated nucleosomes ~7-fold more weakly (data not shown).

Based on the above data, we propose that binding to methylated nucleosomes has two coupled effects: (i) release of ARK loops to directly or indirectly help DNA binding, and (ii) release of two CDs that can bridge nearby nucleosomes (Fig. 4c). This new model revises our previously proposed model [18] (See Supplementary Discussion). Our data implies that the cooperative action of the CD, the CSD-CSD dimer, and the ARK loop, couples the assembly of Swi6 to the recognition of specific features of the nucleosomal template such as H3K9 methylation and nucleosomal DNA. This coupling can ensure correct targeting to H3K9 methylated chromatin and reduce aberrant spread in euchromatin. Interestingly, the loop that stabilizes the auto-inhibited state, assists in binding nucleosomes when in the open state. These mutually exclusive roles of the loop may enable switch-like behavior in HP1 spreading.

To test the significance of this model *in vivo*, we investigated the impact of the LoopX and AcidicX mutants in assembling a functional heterochromatin structure. As these mutants concomitantly weaken oligomerization and nucleosome binding, we expected to observe loss-of-function effects *in vivo*. We first investigated effects on the silencing of a *ura4+* reporter gene inserted at the pericentromeric *imr* region (Fig. 4d). Both mutants show defects in silencing that are comparable to the *swi6+* deletion strain and that are not due to reductions in protein levels (Fig. 4d, and Supplementary Fig. 9). Next, we investigated effects at endogenous centromeric *dg* repeats. In the absence of the RNA interference (RNAi) machinery, Swi6 is important for maintaining high levels of H3K9 methylation at *dg* repeats [27]. While deletion of RNAi components causes a small but reproducible decrease in H3K9 methylation, further deletion of *swi6* causes a much larger decrease in H3K9 methylation [27]. We find that the *loopX* and *acidicX* mutants also show large decreases in H3K9 methylation in the absence of an RNAi component such as dicer (*dcr1*) (Fig 4e and Supplementary Fig. 9). These data imply that the loop-CD interaction is important for the integrity of H3K9 methylated heterochromatin *in vivo*. Our results with the LoopX and AcidicX mutants are also consistent with previous work showing that mutations in these regions affect mitotic stability and mating type switching [17], both of which depend on the integrity of heterochromatin.

The ability of Swi6 to exist in more than one discrete conformational state may allow it to interact with different regulators via the CSD-CSD interface, the hinge or the ARK loop, and this could alter the stability and structure of the Swi6-nucleosome platform (Fig. 4f). The ARKGGG sequence is absent in the other *S. pombe* HP1 protein, Chp2, and this difference may in part explain the different biological roles of Chp2 and Swi6 [28]. In Swi6, the ARK loop stabilizes the auto-inhibited state even though the lysine is not methylated, presumably due to the high effective concentration of the ARK loop relative to its partner CD. However, human HP1α contains just the KG residues of the ARKGGG sequence and, in this context, the lysine can be monomethylated *in vivo* [20]. It is tempting to speculate that the methylation energetically compensates for the loss of the arginine while also making the interaction more regulatable. Protein assemblies that are controlled by release of auto-inhibition have been well-characterized in processes such as actin nucleation and protein tyrosine kinase activation [29,30]. We anticipate that similarly sophisticated mechanisms govern the assembly, spread, and functions of HP1-mediated heterochromatin.

Methods

Protein cloning and purification

Swi6 proteins were purified from *E. coli* as described previously[18]. Except for the CFP-tagged proteins, all other Swi6 protein purifications yield final proteins that are devoid of N- or C-terminal tags. Protein concentrations of all Swi6 construct samples were measured by UV absorption at 280 nm and calculated using the experimentally determined extinction coefficient (see Analytical Ultracentrifugation section). To ensure that there was not any DNA contamination, we measured the 260/280 ratio for every purified protein, which on average it was ~ 0.5.

Reaction Buffer (RB) Conditions

Except where specified, all experiments were performed in the reaction buffer (RB) consisting of 20mM HEPES pH 7.5, 150mM KCl and 1 mM DTT.

Nucleosomes Assembly

Core nucleosomes were assembled on 147 bp of DNA using the 601 positioning sequence, containing a Pst1 site 18 bp in from the 5’ end. For the cryoEM of nucleosomes alone

studies, 207 bp of DNA containing the 601 sequence at one end was used. All nucleosomes were prepared using recombinant *Xenopus laevis* histones and assembled as described previously[31]. Methyl Lysine Analog (MLA) containing H3 histones at position 9 ($H3K_C9me3$) were prepared as described previously[32].

Tryptophan Fluorescence Studies

The association between Swi6 proteins and the H3 peptides (amino acid 1 to 18) were measured following the increases in the internal fluorescence of W104 (one of the three residues in the aromatic cage) using an ISS K2 fluorimeter at 30°C. Samples containing 200nM Swi6 in RB were mixed with increasing concentrations of each H3 peptide, tri-methylated or unmethylated at lysine 9. After an incubation for 10min at 30°C, the fluorescence of W104 was measured with the incident wavelength of 295 nm. The fluorescence intensity F_{obs} at 330 nm was plotted as a function of peptide concentration. A 1:1 binding model was fit to the data using Graphpad Prism and the following set of equations:

$$F_{obs}=\frac{(F_{max}\,[H3_p]+F_{min}K_d)}{([H3_p]+K_d)}$$

F_{max} is the fluorescence at saturating peptide, F_{min} is the fluorescence in the absence of peptide and [$H3_p$] represents the H3 tail peptide. The obtained K_d values were averaged over three independent sets of data.

Fluorescence Polarization (FP) Studies

Fluorescence polarization based measurements of binding to H3 tail peptides (amino acid 1 to 15), DNA and nucleosomes were performed in RB with 0.01% NP40 at 24°C. 5-10 nM of peptide, DNA or nucleosomes were used and Swi6 concentrations were varied. The binding reaction was incubated for 30 min at 24°C and fluorescence polarization was measured using a Molecular Devices HT Analyst with excitation and emission wavelengths of λ_{ex} =480nm and λ_{em} =530nm, respectively. The H3 peptide were labeled at the N-terminus with a fluorescein probe (FAM). The peptide was synthesized by Genscript Piscataway, NJ, USA. The 20mer DNA used in the DNA binding assay was 5' labeled with 5,6 carboxy-fluorescein (IDT). The DNA to assemble fluorescent nucleosomes was labeled on one end by amplifying the sequence using PCR with a primer covalently linked to 6-carboxyfluorescein by a 6-carbon linker (IDT).

All the data were analyzed using Graphpad Prism.

The peptide and DNA binding data were fit by the following equation:

$$F_{obs}=\frac{(F_{max}\,[Swi6]+F_{min}K_d)}{([Swi6]+K_d)}$$

F_{abs} is the fluorescence polarization signal observed, F_{min} is the fluorescence polarization signal for the probe alone (peptide or DNA), and F_{max} is the fluorescence polarization signal at saturating [*Swi6*]. The obtained K_d values were averaged over three or more independent sets of data.

The following model was used to fit the nucleosome binding data to account for Swi6-Swi6 oligomerization that is scaffolded by the Swi6-nucleosome complex. Because the

fluorescent probe is located only on one-end of the DNA (green star), we made the assumption that changes in fluorescence polarization reflect binding of Swi6 on one-side of the nucleosome. We hypothesized that binding to the other side occurs independently and it is invisible to our assay:

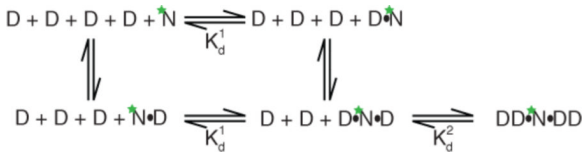

D indicates a Swi6 dimer, D·N·D is the Swi6 nucleosome complex, and D·D·N·D·D is the Swi6 nucleosome complex bound by additional Swi6 dimers. The FP nucleosome data were fitted using the following equation:

$$F_{obs}=\frac{\left(F_0K_d^1K_d^2+F_1\left[Swi6\right]K_d^2+F_2\left[Swi6\right]^2\right)}{\left(K_d^1K_d^2+\left[Swi6\right]K_d^2+\left[Swi6\right]^2\right)}$$

where F_{obs} is the fluorescence polarization signal observed, F_0 is the fluorescence polarization signal for the nucleosome alone, F_1 is the fluorescence polarization signal of the saturated Swi6-nucleosome complex, F_2 is the fluorescence polarization signal of due to the oligomerization of Swi6 scaffolded by the Swi6-nucleosome complex, K_d^1 is the dissociation constant for the Swi6-nucleosome complex, and K_d^2 is the dissociation constant for Swi6-Swi6 scaffolded by the Swi6:nucleosome complex. Data comparing Swi6 WT to the mutants were globally analyzed: the F_0, F_1 and F_2 were fix among all proteins while the K_d^1 and K_d^2 were floated.

Analytical Ultracentrifugation (AUC) Studies

Swi6 proteins were individually dialyzed into RB overnight. Swi6 proteins were quantified by UV absorption at 280nm. We experimentally determined $Swi6^{WT}$ extinction coefficient by recording both interference fringes and UV absorbance at 280nm for a given Swi6 sample. We then converted the number of interference fringes observed into mg Swi6/ml using an average refractive increment of 4.1 fringes/mg/ml. Using this estimated concentration and the absorbance value at 280nm, we then calculated the extinction coefficient at 280nm to be 36,880 M^{-1} cm^{-1}. Simultaneous detection of protein by UV at multiple wavelengths allowed for the determination of the extinction coefficients at 230nm and 250nm (13,650 M^{-1} cm^{-1} and 221000 M^{-1} cm^{-1}, respectively).

All sedimentation experiments were conducted using an analytical ultracentrifuge (Beckman Coulter, Brea, CA) equipped with either sole absorption optical scanner (Optima XLA) or both absorption and interference optics scanner (Optima XLI). Data were acquired with Proteomelab data acquisition software 5. Global analysis of SE and SV isotherm data was performed using the SEDPHAT software. Error estimates were calculated based on replicates of three or more experiments and confidence intervals based on F-statistics and the error projection method. Partial-specific volume (ν), solution density (ρ), solution viscosity (η) were calculated in SEDNTERP.

Sedimentation Equilibrium (SE)—Sedimentation equilibrium experiments were conducted at 8°C in an Optima XLI/A at rotor speeds of 6K, 11K, and 18K rpm in double-

sector centerpieces with sample volumes of 170 μl. Loading concentration of Swi6, in monomer units, was varied from 1.7μM to 32μM. Absorbance data, at wavelengths of 280, 250, and 230nm, and IF data were acquired from samples at five different loading concentrations at all rotor speeds. Global analysis of data at different wavelengths and rotor speeds was conducted with the software SEDPHAT, using Boltzmann exponentials representing the predicted concentration profiles of each species in chemical equilibrium, with amplitudes at all radii constrained by the mass action law:

$$c_{tot}=c_1+nKc_1^n+\sum_{i=1}^{\infty}(n+im)\,Kc_1^n(Lc_1^n)^i$$

in combination with the method of implicit mass conservation, using the bottom position of each solution column as an adjustable parameter. In the above equation, c_{tot} is the total protein concentration, c_1 is the concentration of Swi6 monomer, n is the number of Swi6 subunits that self-associate in the first-step of association (n=2 for dimer formation), m is the molecularity of the chain elongation unit (m=2 for a dimeric chain elongation unit), K is the association constant for Swi6 dimerization (Kd_{obs}^{dim}), L is the association constant for Swi6 isodesmic chain elongation (Kd_{obs}^{iso}). Summation of terms was carried out to a relative numerical precision of 10^{-6}.

Sedimentation Velocity (SV)—Samples volumes of 400μl at an overall final OD between 0.1 and 1.0, were pipetted into double-sector centerpieces, and inserted in an 8-hole rotor, which was placed in the temperature pre-equilibrated AUC chamber. An additional incubation period of 1-2 hours was added with the rotor at rest and under vacuum for temperature equilibration. For experiments performed at 4°C, the samples were left equilibrating under vacuum overnight. Runs were performed at a rotor speed of 50,000 rpm for more than 12 hours. Scans were collected following UV at 230, 250 and 280nm, scanned with a radial step size of 0.003 cm in continuous mode, and/or using the interference system. Data were analyzed using a *c*(*s*) continuous distribution of Lamm equation solutions with the software SEDFIT, followed by integration and assembly into an isotherm of weighted-average s-values. The isotherm was modeled in SEDPHAT with mass action based models for the weighted-average s-value

$$s_w\,(c_{tot})=\left[c_1s_1+nKc_1^ns_n+\sum_i(n+im)\,Kc_1^n(Lc_1^m)^is_n\left(\left(\frac{n+im}{n}\right)\right)^k\right]\frac{1}{c_{tot}}\,(1-k_sc_{tot}M_1)$$

assuming a power law for the sedimentation coefficients of oligomeric species with $\varkappa$ = 0.566 (consistent with increasingly elongated oligomers; this value was pre-determined from the global fit of SE and SV on an extensive data set), in combination with an overall hydrodynamic non-ideality term of magnitude k_s = 0.01 ml/g. As in the equation above, c_{tot} is the total protein concentration, c_1 is the concentration of Swi6 monomer, n is the number of Swi6 subunits that self-associate in the first-step of association (n=2 for dimer formation), m is the molecularity of the chain elongation unit (m=2 for a dimeric chain elongation unit), K is the association constant for Swi6 dimerization (Kd_{obs}^{dim}), L is the association constant for Swi6 isodesmic chain elongation (Kd_{obs}^{iso}), s_1 is the sedimentation coefficient of Swi6 monomer and s_n sedimentation coefficient of Swi6 dimer (n=2).

Rationale for different temperatures—(i) To obtain a model for Swi6 self-association we performed SE and SV AUC studies at 8°C. SE experiments are ~1 week long, so a

temperature of 8°C was used to stabilize the protein. Global analysis of both SE and SV AUC at 8°C allowed us to obtain a thermodynamic information for Swi6 self-association as well as hydrodynamic parameters for Swi6 monomer, dimer and oligomers that were used in all the SV experiments performed at higher temperatures.

(ii) To compare dimerization properties between Swi6 mutants, we had to perform the experiments at 30°C because dimerization is too tight at lower temperatures.

(iii) To stabilize probe-labeled Swi6 proteins, the EPR and AUC experiments were done at 4°C.

Electron Paramagnetic (EPR) Studies

EPR measurements were performed with a Bruker Instruments EMX EPR spectrometer (Billerica, MA). First derivative, X-band spectra were recorded in a high-sensitivity microwave cavity using 50-s, 100-Gauss wide magnetic field sweeps. The instrument settings were as follows: microwave power, 25 mW; time constant, 164 ms; frequency, 9.83 GHz; modulation, 1 Gauss at a frequency of 100 kHz. Each spectrum used in the data analysis was an average of 10-40 50 seconds sweeps from an individual experimental preparation. $Swi6^{3S}$ was labeled by reacting the sole cysteine residue (either K94C or G95C) with the EPR probe 4-maleimido-2,2,6,6-tetramethyl-1-piperidinyloxy (MSL, Sigma Aldrich, St. Louis, MO). The protein was first dialyzed overnight in RB without DTT. It was then incubated with MSL using a 2–fold molar excess of MSL to protein concentration. The mixture was then left to react for 4 hrs at 4°C. The excess label was removed by a microcon concentrator, followed by an additional overnight dialysis step into the above buffer. The protein sample was incorporated into a 25μl capillary and the EPR spectrum was recorded. The temperature of the sample was controlled by blowing dry air (warm or cool) into the cavity and monitored using a thermistor placed close to the experimental sample. To stabilize the $Swi6^{probe}$ WT and mutants we performed the EPR and AUC experiments at 4°C.

The spectra were deconvoluted into mobile and immobile spectral components using the protocols of Purcell *et al*[34].

Electron Microscopy (EM) and Image Processing

Negative Stain EM of CFP-Swi6 and Swi6-CFP—Proteins were dialyzed overnight in RB. 2.5mL of CFP-Swi6 at 0.34μM and of Swi6-CFP at 0.1μM was absorbed to a glow-discharged copper grid coated with carbon film for 30 seconds followed by conventional negative stain with 0.75% uranyl formate. Images were collected using a Tecnai T12 microscope (FEI company, Hillsboro, OR) with a LaB_6 filament and operated at 120 kV accelerating voltage. All images were recorded at a magnification of 67,000 with an UltraScan 4096 × 4096 pixel CCD camera (Gatan Inc, USA).

All images were 2×2 pixel binned to the final pixel size of 3.46Å before any further processing. A total of 5000 and 3000 particles for CFP-Swi6 and Swi6-CFP respectively were selected from ~50 images using the display program SamViewer (written by Maofu Liao). All subsequent image processing was performed using SPIDER [35] and FREALIGN[36].

Cryo-EM Studies of the nucleosome and Swi6-nucleosome complex—Cryo-EM data were collected using Tecnai TF20 electron microscope equipped with a field emission gun (FEI Company, USA) and operated at 120kV (for the nucleosome) or at 200kV (for the Swi6-nucleosome complex). Images were collected at a nominal magnification of 62 kX using a TemF816 8K × 8K CMOS camera (TVIS, Germany).

Nucleosome alone—The nucleosome contained 60 bp of flanking DNA (147 bp of 601 sequence+60 bp extra DNA) and did not contain the MLA on H3K9. All images were binned by a factor of 2 (2.39 Å/pixel) for further processing. Defocus values were determined for each micrograph using CTFFIND [37] and ranged from −1.5um to −3um. A total of 13629 particles were selected and classified into 100 2D-class averages. 3D reconstructions were calculated and refined using GeFREALIGN. The initial model was generated by filtering the atomic structure of the nucleosome (PDB 1KX5) to 35Å (command pdb2mrc from EMAN package)[38]. The resolution was estimated to be ~16.5Å, based on Fourier Shell Correlation (FSC) = 0.5 criteria.

Swi6:H3K$_C$9me3 nucleosome complex—Swi6 was dialyzed overnight in RB. The binding reaction was set such that a) both nucleosome and Swi6 concentrations were above the K_d value measured by FP and b) the Swi6 concentration was sufficient to titrate all the nucleosomes as assayed by native gel shift. Those same conditions were used previously to measure the stoichiometry of the complex by SV AUC and are known to result in homogenous samples[18]. A total of 5,000 particles were selected and classified into 200 2D-class averages and all were included in the final 3D reconstruction. The cryo-EM 3D reconstruction of the nucleosome alone was low pass filtered to 35Å and used as the initial model for 3D refinement of the complex. We used our previous biochemical knowledge to guide the structural analysis. We have previously shown that the complex of Swi6 with an H3K9 methylated nucleosome contains two Swi6 dimers[18]. Given the pseudo-two fold symmetry in the positions of the H3 tails, the simplest model posits that the Swi6 dimers also bind in a pseudo-symmetric manner with one dimer on either side of the nucleosome. Indeed in some of the 2-D class averages we observe density on either side of the nucleosome consistent with the predictions of the biochemical analysis (Supplementary Figure 7). We therefore applied 2-fold symmetry to obtain the 3D reconstruction. The resolution of the final 3D reconstruction was estimated to be ~25Å, based on Fourier Shell Correlation (FSC) = 0.5 criteria. This same resolution was also obtained when the cryo-EM 3D reconstruction of nucleosome alone was low pass filtered to 60Å.

All 3D reconstructions were visualized by UCSF Chimera. The “Fit in Map” function of Chimera was used to dock the atomic structure of the nucleosome (PDB 1KX5) into the 3D volume[39].

To calculate the difference map, the nucleosome alone and the Swi6-nucleosome complex maps were low-pass filtered to 25Å. The difference map was calculated by subtracting the nucleosome from the Swi6-nucleosome complex using the program diffmap.exe (provided by Nikolaus Grigorieff, Brandeis University), which normalizes the density maps before calculating the difference map. The extended shape of the difference density is compatible with the shape of the Swi6 dimer visualized in the negatively stained CFP-Swi6 dimer (Fig. 3a). Such similarity suggested a model for the arrangement of the individual domains of Swi6 and enabled us to manually place the known crystal structures of the CD and CSD into the difference density (Fig.3d).

Silencing Assays

The strains were grown overnight to saturation and diluted to OD_{600} of 1 at the highest dilution. Serial dilutions were performed with dilution factor of 5 and cells were grown on non-selective (YS) and 5-FOA (2 grams/liter of 5-fluoroorotic acid) containing media for *ura4+* reporter at 30°C for 2-3 days.

Quantifying Swi6 protein levels*in vivo*

Swi6 protein levels were quantified using polyclonal antibodies raised in Rabbits by injecting recombinant Swi6.

Chromatin Immunoprecipitation

The ChIP assay was performed as described previously [40]. Cells were lysed at 4°C by bead beating 7 times for 1 min each with 2 min rests on ice. Chromatin fraction was sonicated 20 times for 30s each with 1-min rest in between cycles using Bioruptor. Ab1220 (Abcam) was used for H3K9me2 ChIP and Protein A Dynabeads were used in the washing steps.

Supplementary Material

Refer to Web version on PubMed Central for supplementary material.

Acknowledgments

We thank J. Tretyakova for preparation of histone proteins and J. Leonard for sample preparation for Cryo-EM of nucleosome alone. We thank W. Lim, M. Simon, K. Armache, J. Zalatan, L. Racki and members of the Narlikar laboratory for helpful discussions. DC would like to thank Idelisse Ortiz Torres and Kristopher M. Kuchenbecker for useful scientific discussions and members of the Schuck laboratory for advice on AUC approaches. This work was supported by a grant from the Hillblom foundation to D.C., by grants from the American Cancer Society and Leukemia and Lymphoma Society to G.J.N, NIH grant R01GM071801 to H.D.M. and by a New Technology Award to Y.C. from the UCSF Program for Breakthrough Biomedical Research. P.S. was supported by the Intramural Research Program of NIBIB, National Institutes of Health. N.N. and E.P. were supported by the NIH grant AR053720.

References

1. Eissenberg JC, Elgin SC. The HP1 protein family: getting a grip on chromatin. Current opinion in genetics & development. 2000; 10:204–10. [PubMed: 10753776]
2. Lachner M, O'Carroll D, Rea S, Mechtler K, Jenuwein T. Methylation of histone H3 lysine 9 creates a binding site for HP1 proteins. Nature. 2001; 410:116–20. [PubMed: 11242053]
3. Nakayama J, Rice JC, Strahl BD, Allis CD, Grewal SI. Role of histone H3 lysine 9 methylation in epigenetic control of heterochromatin assembly. Science (New York, NY). 2001; 292:110–113.
4. Noma K, Allis CD, Grewal SI. Transitions in distinct histone H3 methylation patterns at the heterochromatin domain boundaries. Science (New York, NY). 2001; 293:1150–1155.
5. Grewal SIS, Jia S. Heterochromatin revisited. Nature reviews Genetics. 2007; 8:35–46.
6. Hall IM, et al. Establishment and maintenance of a heterochromatin domain. Science (New York, N.Y.). 2002; 297:2232–7.
7. Bannister AJ, et al. Selective recognition of methylated lysine 9 on histone H3 by the HP1 chromo domain. Nature. 2001; 410:120–124. [PubMed: 11242054]
8. Jacobs SA, Khorasanizadeh S. Structure of HP1 chromodomain bound to a lysine 9-methylated histone H3 tail. Science (New York, NY). 2002; 295:2080–2083.
9. Nielsen PR, et al. Structure of the HP1 chromodomain bound to histone H3 methylated at lysine 9. Nature. 2002; 416:103–7. [PubMed: 11882902]
10. Yamada T, Fukuda R, Himeno M, Sugimoto K. Functional domain structure of human heterochromatin protein HP1(Hsalpha): involvement of internal DNA-binding and C-terminal self-association domains in the formation of discrete dots in interphase nuclei. J Biochem. 1999; 125:832–7. [PubMed: 10101299]
11. Brasher SV, et al. The structure of mouse HP1 suggests a unique mode of single peptide recognition by the shadow chromo domain dimer. The EMBO journal. 2000; 19:1587–97. [PubMed: 10747027]

12. Cowieson NP, Partridge JF, Allshire RC, McLaughlin PJ. Dimerisation of a chromo shadow domain and distinctions from the chromodomain as revealed by structural analysis. Current biology : CB. 2000; 10:517–25. [PubMed: 10801440]
13. Smothers JF, Henikoff S. The HP1 chromo shadow domain binds a consensus peptide pentamer. Current biology : CB. 2000; 10:27–30. [PubMed: 10660299]
14. Mendez DL, et al. The HP1a disordered C terminus and chromo shadow domain cooperate to select target peptide partners. Chembiochem : a European journal of chemical biology. 2011; 12:1084–1096. [PubMed: 21472955]
15. Zhao T, Heyduk T, Allis CD, Eissenberg JC. Heterochromatin protein 1 binds to nucleosomes and DNA in vitro. The Journal of biological chemistry. 2000; 275:28332–8. [PubMed: 10882726]
16. Keller C, et al. HP1(Swi6) Mediates the Recognition and Destruction of Heterochromatic RNA Transcripts. Molecular cell. 2012 doi:10.1016/j.molcel.2012.05.009.
17. Wang G, et al. Conservation of heterochromatin protein 1 function. Molecular and cellular biology. 2000; 20:6970–6983. [PubMed: 10958692]
18. Canzio D, et al. Chromodomain-Mediated Oligomerization of HP1 Suggests a Nucleosome-Bridging Mechanism for Heterochromatin Assembly. Molecular cell. 2011; 41:67–81. [PubMed: 21211724]
19. Frigon R, Timasheff S. Magnesium-induced self-association of calf brain tubulin. 2. Thermodynamics. Biochemistry. 1975; 14:4567–4573. [PubMed: 1182104]
20. LeRoy G, et al. Heterochromatin protein 1 is extensively decorated with histone code-like post-translational modifications. Molecular & cellular proteomics : MCP. 2009; 8:2432–2442. [PubMed: 19567367]
21. Sampath SC, et al. Methylation of a histone mimic within the histone methyltransferase G9a regulates protein complex assembly. Molecular cell. 2007; 27:596–608. [PubMed: 17707231]
22. Ruan J, et al. Structural basis of the chromodomain of Cbx3 bound to methylated peptides from histone h1 and G9a. PloS one. 2012; 7:e35376. [PubMed: 22514736]
23. Rice S, et al. A structural change in the kinesin motor protein that drives motility. Nature. 1999; 402:778–784. [PubMed: 10617199]
24. Dawson MA, et al. JAK2 phosphorylates histone H3Y41 and excludes HP1alpha from chromatin. Nature. 2009; 461:819–822. [PubMed: 19783980]
25. Lavigne M, et al. Interaction of HP1 and Brg1/Brm with the globular domain of histone H3 is required for HP1-mediated repression. PLoS genetics. 2009; 5:e1000769. [PubMed: 20011120]
26. Richart AN, Brunner CIW, Stott K, Murzina NV, Thomas JO. Characterization of chromoshadow domain-mediated binding of heterochromatin protein 1α (HP1α) to histone H3. The Journal of biological chemistry. 2012; 287:18730–7. [PubMed: 22493481]
27. Sadaie M, Iida T, Urano T, Nakayama J-I. A chromodomain protein, Chp1, is required for the establishment of heterochromatin in fission yeast. The EMBO journal. 2004; 23:3825–35. [PubMed: 15372076]
28. Sadaie M, et al. Balance between distinct HP1 family proteins controls heterochromatin assembly in fission yeast. Molecular and cellular biology. 2008; 28:6973–6988. [PubMed: 18809570]
29. Mullins RD. How WASP-family proteins and the Arp2/3 complex convert intracellular signals into cytoskeletal structures. Current opinion in cell biology. 2000; 12:91–96. [PubMed: 10679362]
30. Huse M, Kuriyan J. The conformational plasticity of protein kinases. Cell. 2002; 109:275–282. [PubMed: 12015977]
31. Luger K, Rechsteiner TJ, Richmond TJ. Preparation of nucleosome core particle from recombinant histones. Methods In Enzymology. 1999; 304:3–19. [PubMed: 10372352]
32. Simon, MD. Ausubel, Frederick M., editor. Installation of site-specific methylation into histones using methyl lysine analogs.. Current protocols in molecular biology. 2010. [et al.] Chapter 21, Unit 21.18.1–10
33. Vistica J, et al. Sedimentation equilibrium analysis of protein interactions with global implicit mass conservation constraints and systematic noise decomposition. Analytical biochemistry. 2004; 326:234–256. [PubMed: 15003564]

34. Purcell TJ, et al. Nucleotide pocket thermodynamics measured by EPR reveal how energy partitioning relates myosin speed to efficiency. Journal of molecular biology. 2011; 407:79–91. [PubMed: 21185304]

35. Frank J, et al. SPIDER and WEB: processing and visualization of images in 3D electron microscopy and related fields. Journal of structural biology. 1996; 116:190–199. [PubMed: 8742743]

36. Li X, Grigorieff N, Cheng Y. GPU-enabled FREALIGN: accelerating single particle 3D reconstruction and refinement in Fourier space on graphics processors. Journal of structural biology. 2010; 172:407–412. [PubMed: 20558298]

37. Mindell JA, Grigorieff N. Accurate determination of local defocus and specimen tilt in electron microscopy. Journal of structural biology. 2003; 142:334–347. [PubMed: 12781660]

38. Ludtke SJ, Baldwin PR, Chiu W. EMAN: semiautomated software for high-resolution single-particle reconstructions. Journal of structural biology. 1999; 128:82–97. [PubMed: 10600563]

39. Pettersen EF, et al. UCSF Chimera--a visualization system for exploratory research and analysis. Journal of computational chemistry. 2004; 25:1605–12. [PubMed: 15264254]

40. Rougemaille M, Shankar S, Braun S, Rowley M, Madhani HD. Ers1, a rapidly diverging protein essential for RNA interference-dependent heterochromatic silencing in Schizosaccharomyces pombe. The Journal of biological chemistry. 2008; 283:25770–3. [PubMed: 18658154]

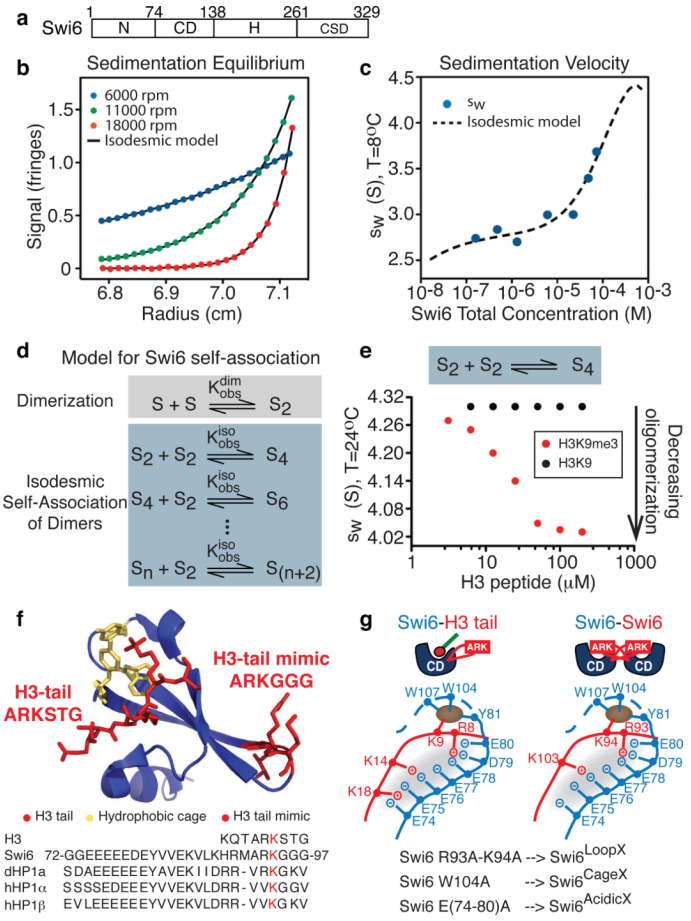

Figure 1. Dissecting Swi6 self-association equilibria

a, Swi6 domains. N: N-terminal region; CD: chromodomain; H: Hinge; CSD: chromoshadow domain. **b,** Sedimentation Equilibrium (SE) AUC analysis of $Swi6^{WT}$ self-association. Interference profiles at different rotor speeds shown. Every 20^{th} point is shown. **c,** Sedimentation Velocity (SV) AUC analysis of $Swi6^{WT}$ self-association. . For b, and c, best fits for global analysis using an isodesmic self-association model are shown. **d,** Model of Swi6 self-association (monomer: S). **e,** [$Swi6^{WT}$] = 20μM. Sedimentation coefficients: dimer (S_2) ~4S; tetramer (S_4) ~5.2S. **f,** Top: Swi6 CD modeled on drosophila HP1 CD with H3K9me3 peptide (PDB: 1KNE). Bottom: H3-tail (aa 4-14) and CD loop regions of Swi6 (aa 72-97), dHP1α, hHP1α and hHP1β. Conserved lysine in red. **g,** Top: Models for CD-CD and CD-loop interactions. H3 tail: green line; methylation: red circle. Middle: Schematic of Swi6:H3 tail interactions (Left) and of hypothetical CD:CD interactions (Right). Grey oval: region of negative charge; brown oval: π-cation interactions. Bottom: mutants used.

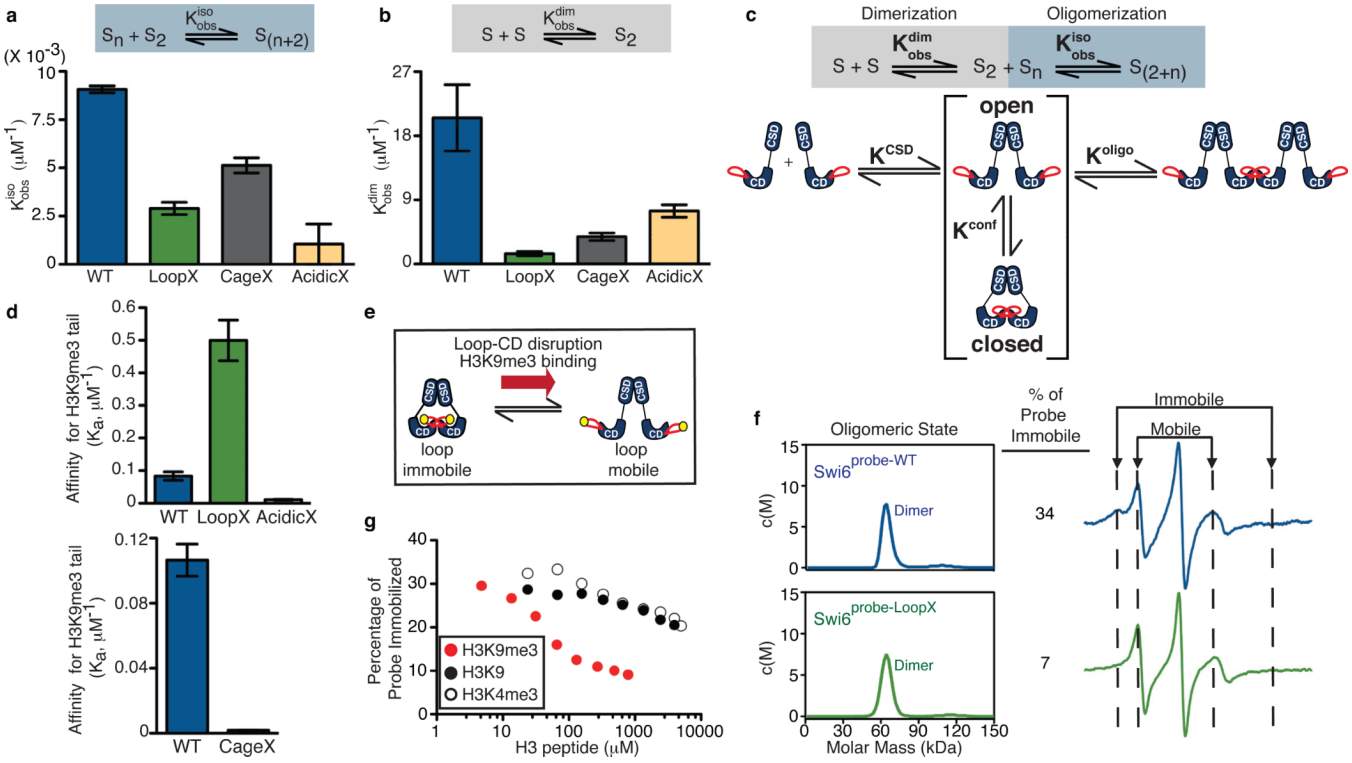

Figure 2. Impact of disrupting H3 tail mimic-CD interaction

a, Isodesmic association constant (K_{obs}^{iso}) and **b,** dimerization association constant (K_{obs}^{dim}) for Swi6 mutants (Values in Supplementary Figure 4). **c,** Model for the self-association of Swi6. (K^{conf} = [open]/closed]). K^{oligo} is isodesmic association constant for oligomerization from the open state. For Swi6$^{\mathrm{WT}}$, $K_{obs}^{\mathrm{dim}}=\frac{K^{csd}}{K^{conf}}$ and $K_{obs}^{\mathrm{iso}}=K^{conf}\times K^{oligo}$. **d,** Affinity constants for H3K9me3 tail peptide measured by tryptophan fluorescence (top) and fluorescence anisotropy (bottom) studies (Values in Supplementary Figure 8). **e,** Location of MSL probe on G95C (yellow circle). **f,** SV AUC (left panels) and EPR analyses (right panels) of Swi6$^{\text{probe-WT}}$ and Swi6$^{\text{probe-LoopX}}$. Representative EPR spectra shown as derivative of absorbance (y-axis) vs. magnetic field (x-axis) . c(M): molar mass distribution. Errors for probe immobilized < 10%. **g,** Impact of 18mer H3 peptides on probe immobilization. [Swi6$^{\text{probe-WT}}$]= 20μM. For all panels, errors (n > 3) represent s.e.m.

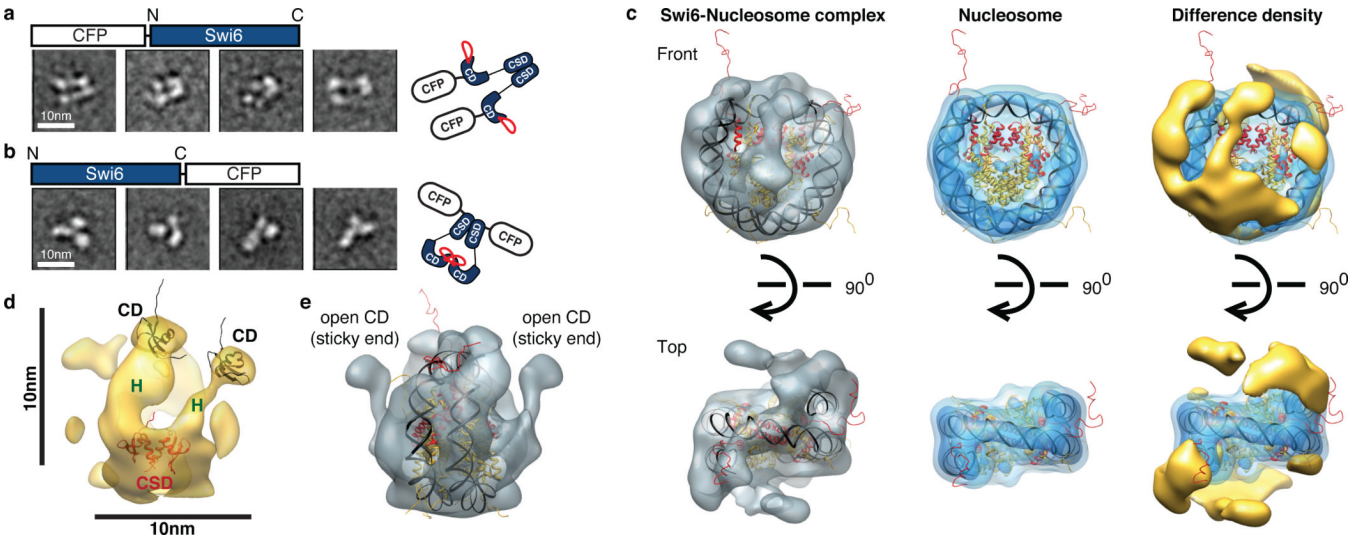

Figure 3. EM studies of Swi6 and Swi6-H3K$_C$9me3 nucleosome complex

a, CFP-Swi6 **.b**, Swi6-CFP. For a, and b, representative 2D class averages are shown. **c,** Two different views of 3D reconstruction of the Swi6:H3K$_C$9me3 nucleosome complex (left), nucleosome (middle), and difference map between the two reconstructions (right). Nucleosome crystal structure (PDB 1KX5) was fitted into reconstruction. Isosurface of nucleosome 3D reconstruction at high threshold in dark blue, and low threshold in light blue (nucleosome type used in methods); H3 in red; difference map in yellow. **d,** Putative locations of Swi6 domains docked into difference map: CD of Swi6 (black; PDB 2RSO, aa 72-142), CSD domain of Swi6 (red; PDB 1E0B), and Hinge (H). **e.** Proposed locations of the two unoccupied CDs.

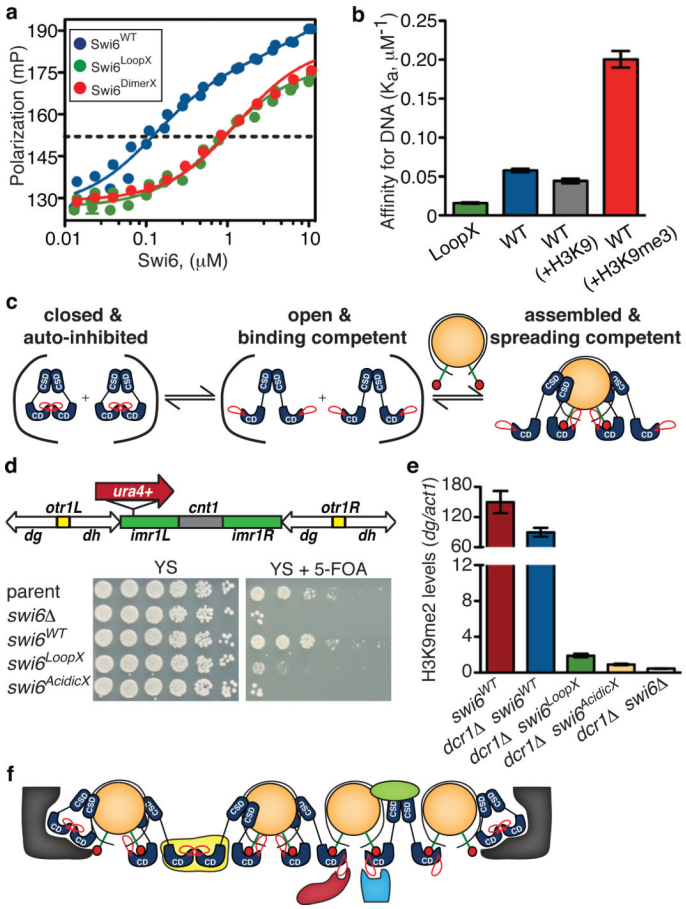

Figure 4. Nucleosome recognition and *in vivo* impact of disrupting loop-CD interaction

a, Nucleosome binding assayed by fluorescence anisotropy. **b,** Affinity constants for 20mer DNA. For a, and b, K_d values are in Supplementary figure 8. Errors (n ≥ 3) represent s.e.m. **c,** Model for conformational switch in Swi6 upon binding methylated nucleosomes. **d,** Top: Schematics of centromere 1 showing *ura4+* reporter. Bottom: Silencing assay using *ura4+* reporter. **e,** swi6^{LoopX} and swi6^{AcidicX} mutants decrease H3K9 methylation levels at the centromeric *dg* in *dcr1Δ* background. Errors: s.e.m from three independent IPs. **f,** Model: Conformational versatility of HP1-chromatin platform enables recruitment of diverse regulators that promote (yellow, red, blue and green cartoons) or inhibit (grey cartoon) heterochromatin spread.